Pergamon

Int. J. Heat Mass Transfer. Vol. 37, No. 5, pp. 753–762, 1994

0017–9310/94 $6.00+0.00

A heat pipe transient analysis model

J.-M. TOURNIER and M. S. EL-GENK

Institute for Space Nuclear Power Studies, Department of Chemical and Nuclear Engineering, The University of New Mexico, Albuquerque, NM 87131, U.S.A.

(*Received* 11 *May* 1993 *and in final form* 5 *October* 1993)

Abstract—A two-dimensional, heat pipe transient analysis model, 'HPTAM', is developed for simulating operations of fully-thawed heat pipes. The model is benchmarked using transient experimental data of a horizontal water heat pipe. The calculated steady-state water vapor and wall axial temperature profiles and the transient power throughput are in good agreement with measurements. Also presented and discussed are the calculated axial distributions of liquid and vapor pressures, effective radius of curvature of the liquid meniscus at the liquid–vapor interface, and liquid pooling and recession following step function heatup and cooldown transients of the water heat pipe.

INTRODUCTION

BECAUSE heat pipes are highly reliable and efficient energy transport devices, they are considered for many terrestrial and space applications. Such wide interest stimulated the development of numerous steady-state and transient heat pipe models, which employed a variety of simplifying assumptions. Bowman and Hitchcock [1] and Issacci *et al.* [2] developed two-dimensional transient models of vapor flow in heat pipes and showed that a one-dimensional treatment is inadequate since it could not accurately predict the axial heat and mass transfers or the pressure drop. Such vapor flow models provide valuable information on vapor flow dynamics, however, they are not useful for the design and transient analysis of heat pipes.

Ivanovsky *et al.* [3] and Tilton *et al.* [4] suggested that during steady-state or slow transients, heat pipe operation can adequately be described by the heat balance in the various heat pipe regions. Following this observation, Chang and Colwell [5], Tilton *et al.* [4], Faghri and Chen [6] and Cao and Faghri [7] solved the two-dimensional heat conduction equations for the wall and liquid–wick regions, which were thermally coupled to either a one- or two-dimensional vapor flow model. Faghri and Chen used their steady-state model to evaluate the effects of axial conduction, vapor compressibility and viscous dissipation on the operation of water and sodium heat pipes. Cao and Faghri [8] also modeled the startup of heat pipes from the frozen state. Different startup periods were considered, including free-molecule and continuum vapor flow conditions. Continuum flow was modeled using the two-dimensional compressible Navier–Stokes equations, while the rarefied flow was simulated using a self-diffusion model.

Tilton *et al.* [4], Cao and Faghri [7] and other investigators mentioned above [3–8] neglected both the liquid flow and the hydrodynamic coupling of the liquid and vapor phases by assuming the wick to be a pure conducting medium with an effective thermal conductivity. Later, Faghri and Buchko [9] included the effect of liquid flow in the wick by treating this region as a saturated and isotropic porous medium, but computed the pressure profiles along the heat pipe independently. Such decoupling of the liquid and vapor momentum equations can result in an error when calculating the liquid flow rates and vapor pressure.

Ransom and Chow [10], Doster and Hall [11] and Seo and El-Genk [12] incorporated liquid flow and thermal compressibility, hydrodynamically coupled the liquid and vapor phases, and predicted the vapor volume distribution in the wick. They used the capillary relationship of Pascal to relate the phasic pressures, and the radius of curvature of the liquid meniscus at the liquid–vapor (L–V) interface was geometrically related to the vapor volume fraction in the wick. Such information is needed for predicting the capillary and dryout limits during transient operation of the heat pipe.

Although Ransom and Chow [10], Doster and Hall [11] and Seo and El-Genk [12] have incorporated the effects of liquid flow and thermal compressibility, their models, except that of Doster and Hall, lacked the capability of predicting the liquid pooling at the end of the condenser. Such pooling occurs due to the thermal expansion of the liquid phase during startup transients of heat pipes charged with excess liquid [13]. The pooling model of Doster and Hall deals with local variations of the liquid fraction in the wick region to differences in evaporation/condensation rates and thermal expansion of the liquid. However, it does not determine when and where a 'wet point' appears in the heat pipe nor its propagation with time toward the end of the condenser as the heat pipe continues to heat up (a 'wet point' is where the liquid–vapor interface becomes flat and the vapor and the liquid pressures are equal). This process is described in detail

NOMENCLATURE

a_{cc}	evaporation accommodation coefficient, equation (13)
A_r	interfacial surface area [m^2]
C	Ergun inertia coefficient, equations (2) and (4)
$\bar{\bar{D}}$	deformation rates tensor
F	external acceleration [m s^{-2}]
h	enthalpy [J kg^{-1}]
k	thermal conductivity [W m^{-1} K^{-1}]
K	wick permeability [m^2]
M	molecular weight [kg mol^{-1}]
$\dot{m}$	evaporation/condensation mass flux [kg m^{-2} s^{-1}]
P	pressure [Pa]
Q	conductive heat flux [W m^{-2}]
$\mathbf{Q}$	conductive heat flux vector
R	radius [m], universal gas constant [8.314 J mol^{-1} K^{-1}]
R_c	radius of curvature [m]
R_p	interfacial wick pore radius [m]
r	radial coordinate [m]
T	temperature [K]
t	time [s]
U	mean filter (area-averaged) velocity [m s^{-1}]
$\mathbf{U}$	mean filter velocity vector
V_p	volume of hemispherical pores at liquid–vapor interface [m^3]
z	axial coordinate [m].

Greek symbols

α_p	pore void fraction at liquid–vapor interface
ε	wick volume porosity
μ	dynamic viscosity [kg m^{-1} s^{-1}]
μ_c	cosine of contact angle of liquid meniscus, R_p/R_c
ρ	density of fluid phase [kg m^{-3}]
ρ_m	density of wick matrix [kg m^{-3}]
σ	surface tension [N m^{-1}].

Superscripts/subscripts

a	adiabatic region
c	condenser region
e	evaporator region
int	liquid–vapor interface
j	axial cell number
L	liquid phase
m	wick solid matrix
p	pore
r	radial component
sat	saturation
V	vapor phase
w	wall region
z	axial component.

later in the paper. Similarly, the pool model of Doster and Hall does not handle the accumulation and receeding of the liquid pool with time during the heatup and cooldown transients of the heat pipe, respectively.

The models of Ransom and Chow [10], Doster and Hall [11] and Seo and El-Genk [12] also treated the vapor flow using either a one-dimensional, transient approximation [10, 11] or a quasi-steady state approach [12], which may not be justified during rapid startup or shutdown transients of heat pipes. At startup, when a heat pipe is operating at low vapor density and high vapor velocity, large radial temperature gradients may develop in the wall, liquid–wick and vapor regions, requiring a two-dimensional treatment of the vapor flow [14].

These effects are incorporated in the two-dimensional Heat Pipe Transient Analysis Model (HPTAM) presented in the following section. In addition to developing this model, the objective of this paper is to benchmark the model predictions against recent experimental data of Huang *et al.* [15] for a horizontal water heat pipe. An analysis is performed to determine the transient behavior and axial distributions of the liquid and vapor pressures, the radius of curvature of the liquid meniscus at the liquid–vapor interface, and liquid pooling and recession following step function heatup and cooldown transients of the water heat pipe.

MODEL DESCRIPTION AND GOVERNING EQUATIONS

The model divides the cylindrical heat pipe into three radial regions: wall, liquid–wick, and vapor regions (see Fig. 1(a)) and incorporates several working

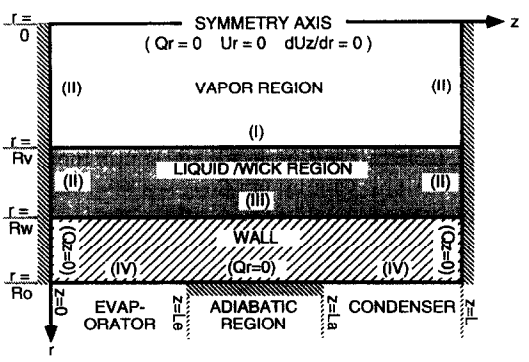

FIG. 1. Physical model of heat pipe and boundary conditions.

fluids, such as lithium, sodium, potassium and water, and structural materials including tungsten, niobium, zirconium, stainless-steel and copper. Future additions to the model that are currently being developed include molecular flow and freeze and thaw capabilities. Also, should a chocked flow develop in the vapor region during a heat pipe startup, particularly with liquid metals working fluids, the present model is capable of handling such a condition. The wick can be either an annular wire-screened mesh or a homogeneous porous medium. The flow in the liquid–wick porous region of the heat pipe is modeled using the Brinkman–Forchheimer extended Darcy flow model [16], while the volume-averaged homogeneous model described by Cheng [17] is used to model the heat transfer. The resulting governing equations in the liquid–wick region of the heat pipe are:

Continuity

$$\varepsilon\frac{\partial\rho}{\partial t}+\operatorname{div}(\rho\mathbf{U})=0 \tag{1}$$

Radial momentum balance

$$\frac{1}{\varepsilon}\frac{\partial(\rho U_r)}{\partial t}+\frac{1}{\varepsilon^2}\operatorname{div}(\rho U_r\mathbf{U})+\left[\frac{\mu}{K_r}+\frac{C}{\sqrt{(K_r)}}|\rho\mathbf{U}|\right]U_r = \rho F_r-\frac{\partial P}{\partial r}+\frac{1}{\varepsilon}[\overrightarrow{\operatorname{Div}}(2\mu\bar{\bar{D}})]_r-\frac{2}{3\varepsilon}\frac{\partial}{\partial r}[\mu\operatorname{div}(\mathbf{U})] \tag{2}$$

where

$$[\overrightarrow{\operatorname{Div}}(2\mu\bar{\bar{D}})]_r=\frac{1}{r}\frac{\partial}{\partial r}\left[2\mu r\frac{\partial U_r}{\partial r}\right]-2\mu\frac{U_r}{r^2}+\frac{\partial}{\partial z}\left[\mu\left(\frac{\partial U_r}{\partial z}+\frac{\partial U_z}{\partial r}\right)\right] \tag{3}$$

Axial momentum balance

$$\frac{1}{\varepsilon}\frac{\partial(\rho U_z)}{\partial t}+\frac{1}{\varepsilon^2}\operatorname{div}(\rho U_z\mathbf{U})+\left[\frac{\mu}{K_z}+\frac{C}{\sqrt{(K_z)}}|\rho\mathbf{U}|\right]U_z=\rho F_z-\frac{\partial P}{\partial z}+\frac{1}{\varepsilon}[\overrightarrow{\operatorname{Div}}(2\mu\bar{\bar{D}})]_z-\frac{2}{3\varepsilon}\frac{\partial}{\partial z}[\mu\operatorname{div}(\mathbf{U})] \tag{4}$$

where

$$[\overrightarrow{\operatorname{Div}}(2\mu\bar{\bar{D}})]_z=\frac{\partial}{\partial z}\left[2\mu\frac{\partial U_z}{\partial z}\right]+\frac{1}{r}\frac{\partial}{\partial r}\left[\mu r\left(\frac{\partial U_r}{\partial z}+\frac{\partial U_z}{\partial r}\right)\right] \tag{5}$$

Energy balance

$$\frac{\partial}{\partial t}[\varepsilon\rho h+(1-\varepsilon)(\rho h)_m]+\operatorname{div}(\rho h\mathbf{U})=\frac{\partial P}{\partial t}+U_r\frac{\partial P}{\partial r}+U_z\frac{\partial P}{\partial z}-\operatorname{div}(\mathbf{Q}), \tag{6}$$

where

$$\mathbf{Q}=\left[-k\frac{\partial T}{\partial r},\quad -k\frac{\partial T}{\partial z}\right]. \tag{7}$$

In equations (2) and (4), the inertia coefficient C is calculated using the expression derived by Ergun ($C=0.143\,\varepsilon^{-3/2}$). Ergun [16] used experimental data on the flow of gases through beds of granular solids of various shapes (various-sized spheres, sand and pulverized coal). The effect of viscous dissipation is neglected in equation (6). ε, K_r and K_z are the effective porosity and radial and axial permeabilities of the liquid–wick region, respectively. The well-known transient conduction form of equation (6) is solved in the solid wall region. In the vapor region, equations (1)–(5) are used, but with a porosity of unity and permeabilities of infinity. For a fully-thawed water heat pipe, the vapor phase is assumed to be saturated, therefore there is no need to solve the energy equation for this phase.

The liquid and vapor phases are coupled at the liquid–vapor (L–V) interface. The conservation of the normal mass fluxes at this interface yields:

$$\dot{m}=-\rho_L U_r^L=-\rho_V U_r^V. \tag{8}$$

The normal momentum jump condition at the L–V interface relates the static pressure drop across the interface to the capillary pressure head in the wick and the normal viscous stress discontinuity as [18]:

$$(P_L-P_V)+2\frac{\sigma}{R_c}+\dot{m}^2\left(\frac{1}{\varepsilon\rho_L}-\frac{1}{\rho_V}\right)=2\left[\mu_L\frac{\partial U_r^L}{\partial r}-\mu_V\frac{\partial U_r^V}{\partial r}\right]-\frac{2}{3}[\mu_L\operatorname{div}(\mathbf{U}^L)-\mu_V\operatorname{div}(\mathbf{U}^V)]. \tag{9}$$

Instead of using the transverse momentum jump condition, the model assumes a non-slip condition at the L–V interface (that is, $U_z^L=U_z^V=0$). This assumption is physically acceptable when dealing with viscous phases separated with a solid wire-screened mesh or a homogeneous porous medium. The model also assumes continuous temperature at the L–V interface ($T^L=T^V=T^{int}$).

The enthalpy jump condition at the L–V interface relates the enthalpy change due to evaporation/condensation to the discontinuities of the heat flux as:

$$Q_r^L+\dot{m}(h^V-h^L)=0. \tag{10}$$

In equation (9), the radius of curvature of the liquid meniscus at the interface, R_c, is geometrically related to the amount of vapor in the wick. The maximum capillary pressure head occurs when the radius of curvature of the liquid meniscus is equal to the pore

radius. In this case, the volume of vapor in the wick forms a hemisphere of radius R_p in each pore of the wick. For this condition, the vapor volume in the wick is related to the wick porosity, ε, and pore radius, R_p, by

$$V_p' = \left(\frac{\varepsilon A_r'}{\pi R_p^2}\right)\left(\tfrac{2}{3}\pi R_p^3\right) = \tfrac{2}{3}\pi R_p \varepsilon A_r'. \qquad (11)$$

Assuming hemispherical pores, the void fraction α_p in the wick (the volume of vapor in the wick over the volume of the hemispherical pores) can be expressed in terms of the cosine of contanct angle ($\mu_c = R_p/R_c$) [12] as:

$$\alpha_p = \frac{1}{\mu_c^3}\left[1-\left(1+\frac{\mu_c^2}{2}\right)\sqrt{(1-\mu_c^2)}\right], \qquad (12)$$

where α_p and μ_c vary between 0 and 1. Equation (12) is inversed using the approximations derived by Seo and El-Genk [12].

To account for the thermal resistance at the L–V interface, the evaporation and condensation mass fluxes are calculated from the kinetic theory of gases:

$$\dot{m} = a_{cc}\left(\frac{M}{2\pi R T^{int}}\right)^{1/2}[P_{sat}(T^{int}) - P_v]. \qquad (13)$$

The governing equations and boundary conditions, together with the equations of state of the liquid and vapor phases, thermophysical properties for the wall and both fluid phases, and the initial conditions specified by the user provide all necessary relations to obtain a closed mathematical solution. Equations (1)–(13) are solved subject to the boundary conditions delineated on Fig. 1. The jump conditions (I) are represented by equations (8)–(10), while the boundary conditions (II) and (III) are given, respectively, as

$$Q_x = 0, \quad U_r = U_z = 0,$$

and

$$Q_r^L = Q_r^W, \quad T^L = T^W, \quad U_r^L = U_z^L. \qquad (14)$$

The boundary condition (IV), which can be either isoflux, isothermal, radiative or convective, is applied independently in the evaporator and condenser regions.

LIQUID POOLING MODEL

Figure 2 presents a schematic of the liquid pooling model incorporated in the present effort. During startup of a heat pipe, the temperature of the liquid phase in the evaporator section increases initially rapidly, and hence the working fluid volume increases due to thermal expansion. When the rate of increase in the liquid volume (taking into account vapor condensation in the condenser section) exceeds the liquid flow rate towards the evaporator, the radius of curvature of the liquid meniscus increases. This increase in the radius of curvature causes the L–V interface to

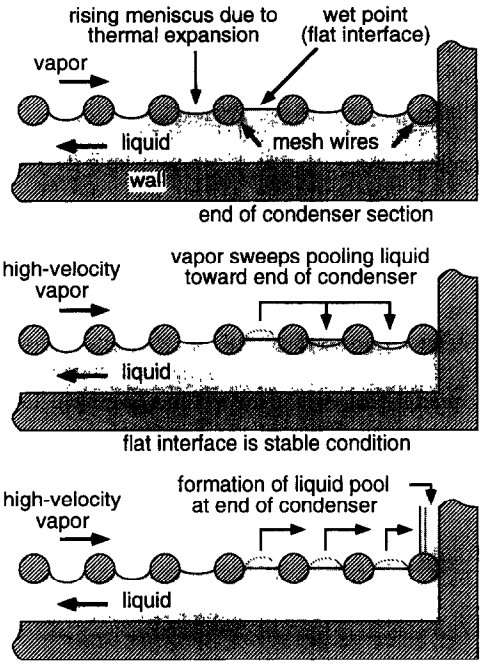

FIG. 2. Illustration of liquid pooling at end of condenser.

eventually flatten at some point along the heat pipe, the so-called wet point as defined by Busse and Kemme [19]. At the wet point, liquid and vapor interfacial pressures are equal and the wick void fraction is zero. Further heating of the heat pipe could cause the liquid meniscus at the wet point to become convex. While such a convex liquid meniscus in the wick might be possible in principle, it probably would not be very stable and the excess liquid will be entrained by the vapor stream, transforming the L–V interface into a flat surface. A liquid pooling submodel in HPTAM assumes that as the transient progresses in time, any excess liquid is swept by the vapor flow towards the end of the condenser, leaving a flat interface and filling up the eventual concave meniscii on its way. Therefore, the wet point moves towards the end of the condenser. When the interface at the end of the condenser eventually flattens, excess liquid accumulates in the vapor core and forms a liquid pool. Experiments performed at Los Alamos by Merrigan *et al.* [13] using a lithium heat pipe have shown that during startup, excess liquid in the heat pipe pools at the end of the condenser and reduces its effective length.

METHOD OF SOLUTION

The governing equations and boundary conditions in HPTAM are discretized using the volume integration method of Patankar [20] and a numerical scheme is developed using the well-known Eulerian staggered-grid. The liquid and vapor velocities are determined at the cell boundaries while the other quantities, such as pressures and enthalpies, are evaluated at the cell center. The numerical solution is

obtained using a predictor/corrector method similar to that proposed by Issa [21]. Only the treatment of the capillary and pooling effects is described in this paper, more details can be found in ref. [22].

In the first step of the numerical algorithm, a procedure similar to the Implicit Continuous-fluid Eulerian technique of Harlow and Amsden [23] is used. The pressure gradient in the conservative forms of the momentum equations is discretized implicitly. The off-diagonal velocity corrections appearing in the diffusion/convection terms are equated to the diagonal velocity correction, as it is done in the SIMPLE-Consistent algorithm of van Doormaal and Raithby [24]. By eliminating the advanced-time mass fluxes appearing in the mass balance equation and considering the pressure variation with the density only, the continuity equation is reduced to the Poisson equation, which is then solved for the pressure field. During this predictor step, liquid and vapor volumes around the L–V interface are treated as functions of the wick void fractions. These void fractions are linearized in terms of the cosines of the contact angles using equation (12). The latter are implicitly related to the liquid and vapor pressures at the L–V interface through the radial momentum jump condition (equation (9)). The densities and radii of curvature of the liquid meniscus for the advanced time are then obtained, with the temporary new-iteration pressures and mass fluxes.

HPTAM handles the liquid-pooling phenomenon described above as follows. When a convex liquid meniscus occurs somewhere along the heat pipe, the interface is assumed flat at this particular location and the radial momentum jump condition at the L–V interface (equation (9)) is used to calculate the pressure in the liquid cell next to the diphasic interface. Then, using the mass balance in this cell, the mass of the excess liquid pooling is determined. This mass is then transported into the next interfacial liquid cell. Once the wet point reaches the end of the condenser, the liquid forms a pool in the vapor core region. The liquid-pooling submodel also simulates liquid pool recession during the subsequent cooldown of the heat pipe.

Finally, during the stabilizing step for the convective and diffusive terms, the momentum conservation equations are solved for the velocity field, and the enthalpy equations are solved for temperatures and evaporation/condensation rates by implicitly coupling equations (10) and (13) at the L–V interface.

DESCRIPTION OF THE WATER HEAT PIPE EXPERIMENT AND MODELING

To verify the system of equations in HPTAM, the model predictions are compared with the transient results of Huang *et al.* [15] for a horizontal water heat pipe experiment. The copper heat pipe, 1.73 cm I.D., 1.91 cm O.D., employs a double-layered, 150 mesh copper screen wick. The lengths of the evaporator, adiabatic, and condenser sections are 60, 9, and 20 cm, respectively. The vapor temperature is measured along the centerline of the heat pipe using a special probe made of a thin walled brass tube (3.2 mm O.D.) instrumented with eleven thermocouples, equally spaced along the heat pipe. An additional eleven thermocouples are attached to the outer surface of the heat pipe wall to measure its temperature at the same axial location as the vapor temperature thermocouples. The evaporator section is uniformly heated using a flexible electric tape and the condenser section is convectively cooled using a water jacket. More details on the heat pipe design and experimental setup are available in ref. [15].

The experimental heat pipe was initially at room temperature (296.2 K) when the electrical power to the heating tape in the evaporator section increased in a step-function to 575 W. The cooling water enters the condenser cooling jacket at 294.5 K and 11.33 g s^{-1}. After about 10 min into the heatup transient, the heat pipe reaches steady-state. At steady-state, the effective power throughput, determined from the heat balance in the condenser cooling jacket, was 443 W. The difference between the electric input to the electric tape and the steady-state effective power throughput (132 W) was approximately equal (within 5%) to the heat losses from the surface of the insulation in the evaporator section to ambient by natural convection [15]. After about 7 min of steady-state operation, the electrical power to the heating tape was turned off, and the heat pipe entered the cooldown phase of the transient.

Because the water flow rate in the cooling jacket is relatively small, a transient one-dimensional water jacket submodel was thermally coupled to the condenser wall in HPTAM in order to calculate the axial distribution of the coolant bulk temperature in the jacket. At steady-state, the convective heat transfer coefficient in the jacket determined from the experiment was 1800 W m^{-2} K^{-1}; this value is used in the model during the simulation. The liquid–wick thickness assumed is 0.75 mm, and wick effective pore radius, porosity and permeability were taken as 54 μm, 0.9 and 1.5×10^{-9} m^2, respectively. The effective thermal conductivity of the liquid–wick region is calculated using the equation given by Chi [25] for distributed cylinders having an effective porosity of 0.5. The evaporation accommodation coefficient in equation (13) was taken as 0.1, and the initial vapor void fraction in the wick was assumed uniform along the heat pipe, with a value of 0.15.

COMPARISON OF THE MODEL WITH WATER HEAT PIPE EXPERIMENT

To account for the actual heat input to the heat pipe evaporator section during the experiment, transient calculations were performed using the measured transient wall temperatures along the evaporator section.

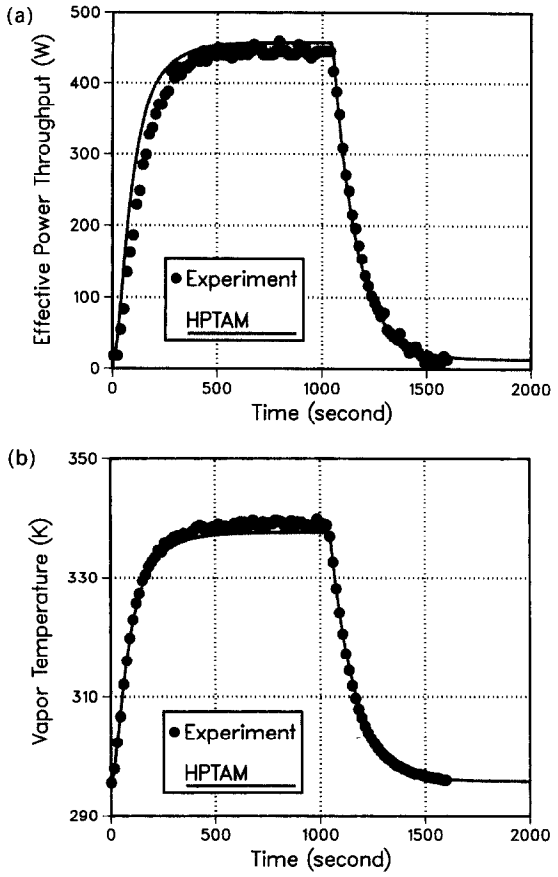

FIG. 3. (a) Comparison of calculated transient response of effective power throughput with water heat pipe experimental data. (b) Comparison of calculated and experimental transient response of vapor temperature for the water heat pipe.

This approach gives a good estimate of the input heat flux in the evaporator region, without the complexity and uncertainty associated with modeling the thermal response of the electric heater and of the insulation along the evaporator section. Comparison with the experimental results confirm the validity of using the transient wall temperatures to determine the heat input to the evaporator region of the heat pipe. In the experiment, the wall temperature in the evaporator section was measured at 7 axial locations and found to be uniform. Figures 3(a) and (b) compare the calculated transient response of the effective power throughput, determined from the heat balance in the cooling jacket, and of the vapor temperature with experimental data. The calculated effective power throughput at steady-state (455 W) is almost the same as that reported in the experiment (443 W). However, the transient reponse of the calculated power throughput is somewhat faster than that in the experiment. This is because in the experiment, a relatively large fraction of the heat generated in the electric tape is initially stored in the insulation surrounding the evaporator and adiabatic sections and in the condenser jacket, therefore slowing down the heat pipe transient. As shown in Fig. 3(b), the calculated transient vapor temperature compares very well with experimental measurements. At steady-state, the calculated vapor temperature was only 1.2 K lower than that measured. Such good agreements at steady-state suggest that the model can predict the thermal resistance of the heat pipe relatively well. Figure 4 compares the calculated wall and vapor temperatures along the heat pipe with those measured at different times during the heatup transient; again the comparison is good. As this figure shows, the calculated vapor temperature is nearly uniform along the heat pipe and in agreement with experimental values. Such agreement between HPTAM and experimental data of the water heat pipe verifies the soundness of the system of equations and the modeling approach used.

WICK VOID FRACTION AND LIQUID POOLING RESULTS

In Fig. 5, the vapor pore void fraction, α_p, is normalized with respect to its initial value of 0.15. At the beginning of the heatup transient, the liquid temperature and volume increase rapidly, causing the vapor void fraction in the wick to decrease at a relatively uniform rate (see Fig. 5). Because of the evaporation and condensation in the heat pipe, the void fraction decreases (or the radius of curvature of the liquid meniscus increases) faster in the condenser than in the evaporator. In the evaporator, liquid evaporation competes with the liquid compressibility effect by removing mass, while condensation adds up to the fluid volume along the condenser. During this period of decreasing wick void fraction, the liquid pressure is lower than the vapor pressure; the pressure difference decreases with time and eventually vanishes after about one minute into the transient (see Fig. 6). At this time, a wet point appears and excess liquid begins to accumulate at the end of the condenser section, forming a water pool (Fig. 7). At the wet point, the L–V interface is flat (or the pore void fraction is zero) and the liquid and vapor total pressures are equal (Figs. 5 and 6). The first wet point appears at the end of the condenser because the full length of the condenser became operational before liquid pooling occurs. The situation would have been different if a larger amount of working fluid had been introduced in the heat pipe [22]. After the formation of the liquid pool, any increase in liquid volume due to thermal expansion is accommodated in the pool (Fig. 7). Essentially, the structure of the L–V interface is governed by evaporation, condensation and liquid flow return. Except in the flooded portion of the condenser, the vapor void fraction recovers along the heat pipe, as shown in Fig. 5. As the effective power throughput in the water heat pipe increases, the pressure losses in the liquid–wick region increase. Also, the wick void fraction at the beginning of the evaporator rises in order to provide the necessary capillary pressure head needed to circulate the liquid in the

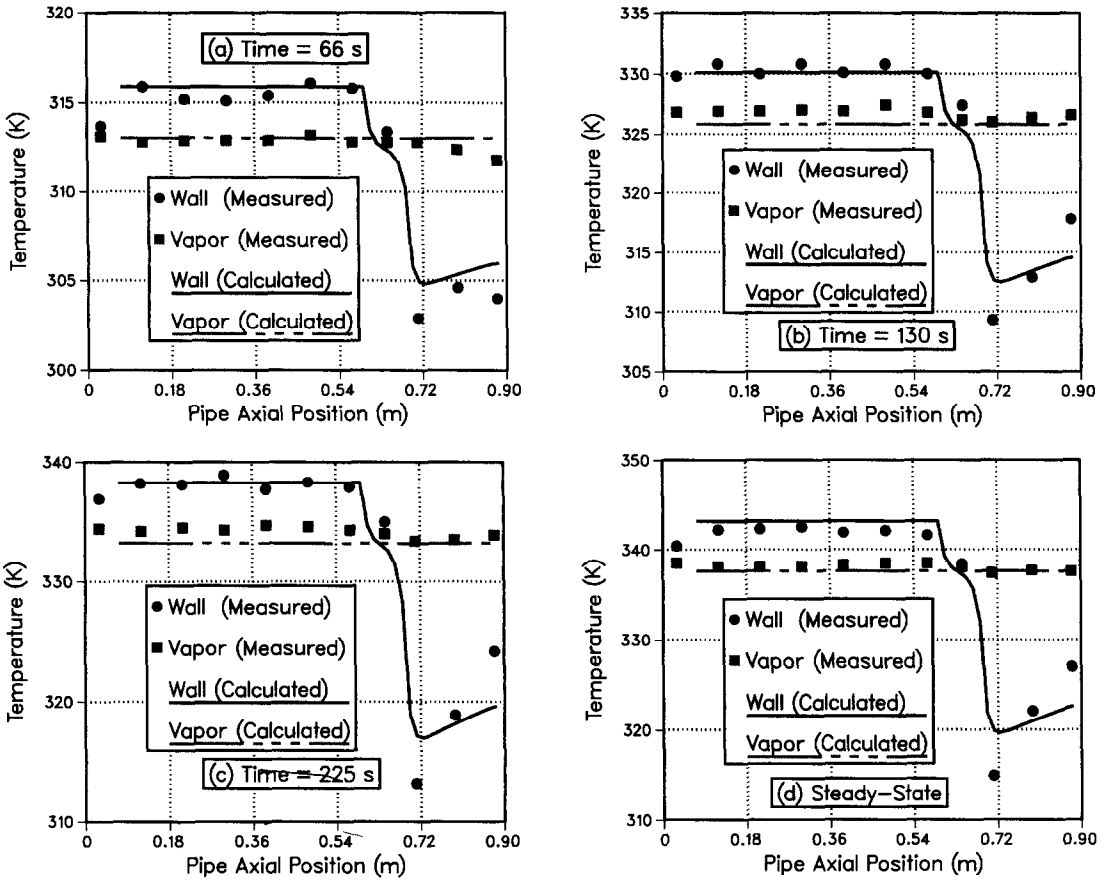

FIG. 4. Comparison of calculated and experimental vapor and wall temperature profiles along the water heat pipe at different times during the heatup transient.

wick region. Before steady-state is reached, the rate of evaporation is greater than the liquid flow return from the condenser to the evaporator. In the condenser, the vapor pressure recovers where the rate of liquid removal is greater than the rate of condensation.

At steady-state, the liquid pool extends to about 1.7 mm (Fig. 7). Figures 8 and 9 show the calculated axial distributions of the liquid and vapor pressures at steady-state. At a power throughput of 455 W, a vapor pressure recovery of 66% occurs along the condenser section. Figure 9 shows that the liquid pressure losses in the wick region are much larger than the vapor pressure losses. This is expected since the liquid is flowing across a relatively tight wire-screen wick. Figure 9 also shows that the vapor and liquid total pressures are equal at the end of the condenser, where it is flooded. As delineated in Fig. 10, at steady-state, the vapor void fraction in the wick is highest (or liquid meniscus radius of curvature is smallest) at the

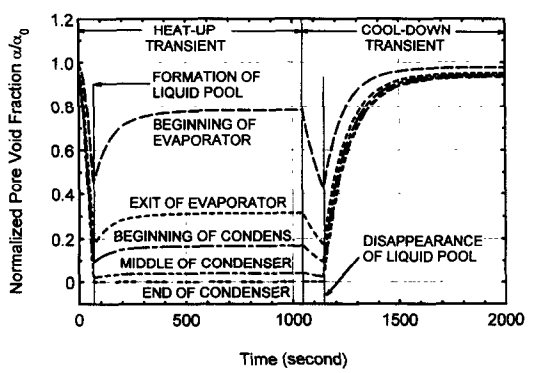

FIG. 5. Calculated normalized vapor void fraction in the wick at different locations along the heat pipe, as a function of time.

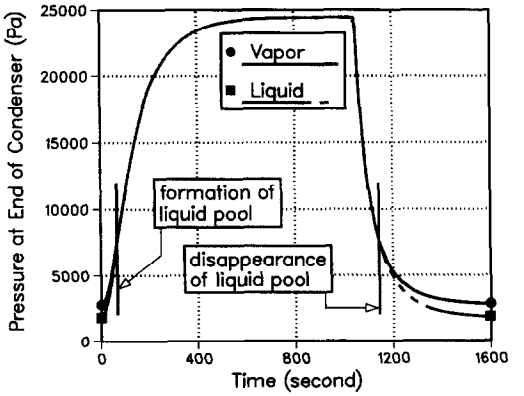

FIG. 6. Calculated liquid and vapor pressures of the water heat pipe as a function of time.

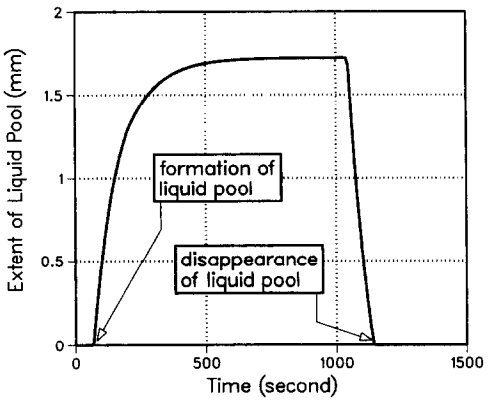

FIG. 7. Extent of liquid pooling at the end of the condenser in water heat pipe as a function of time.

beginning of the evaporator and decreases to zero at the end of the condenser. Figure 11 shows the axial distribution of the evaporation and condensation rates along the heat pipe. At steady-state, evaporation is uniform along the evaporator, while condensation decreases along the condenser due to the increase in temperature along the cooling jacket (Fig. 4). Some evaporation and condensation occurs in the adiabatic section due to the effect of axial conduction in the wall and liquid–wick regions.

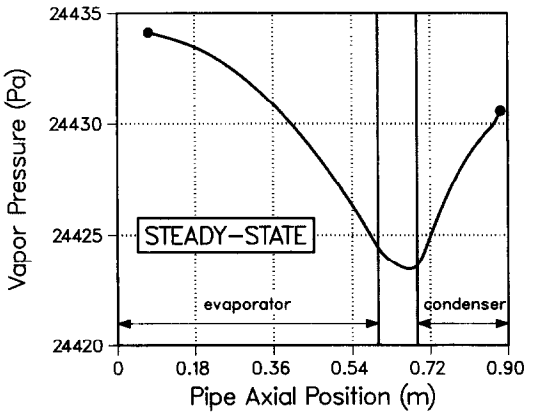

FIG. 8. Calculated axial distribution of the vapor pressure at steady-state.

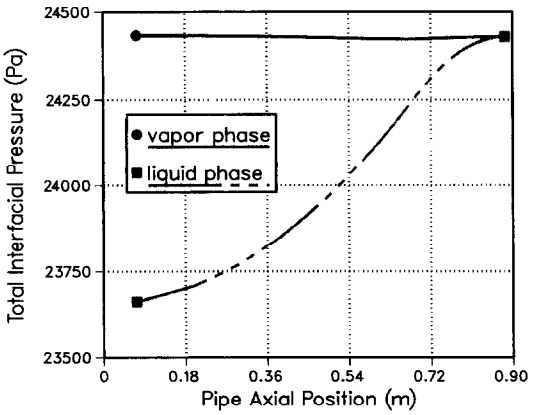

FIG. 9. Calculated axial distributions of the interfacial pressures at steady-state for the water heat pipe.

After 17 min of heatup transient (1040 s), the electrical power to the heating tape was turned off. However, the water was kept running in the cooling jacket. During the first period of the cooldown, the wick void fraction decreases (or the liquid meniscus rises) along the heat pipe, as shown in Figs. 5 and 10. Subsequent decrease in liquid volume due to thermal compressibility causes the liquid pool to receed (Fig. 7). As Fig. 11 shows, the rate of evaporation decreases faster than the rate of condensation, causing the mass of vapor in the heat pipe to decrease with time. This inbalance between evaporation and condensation causes the vapor void fraction in the wick to decrease faster in the condenser than in the evaporator. After 1142 s of the transient, the liquid pool disappears (Fig. 7). From then on, the structure of the L–V interface is generally governed by the thermal compressibility of the liquid phase. Because the liquid temperature and volume decrease rapidly, the vapor void fraction in the wick increases at a relatively uniform rate (see Figs. 5 and 10), and so is the difference between the vapor and liquid pressures (Fig. 6). The difference between the vapor void fraction in the evaporator and the condenser is governed by the evaporation/condensation rates, or the power transported through the heat pipe. As the heat pipe cools down, the wick void fraction along the heat pipe becomes more uniform and returns to its initial value of 0.15.

Figure 12 shows the transient variation of the centerline vapor velocity at the exit of the evaporator. During the heatup and cooldown transients, the vapor velocity increases above its full-power steady-state value of 10 m s^{-1}, for a short period of time. The first peak occurs because the heat transport capability of the heat pipe increases faster than the mass of vapor in the core. The second peak occurs at the beginning of the cooldown phase and is related to the inbalance between evaporation and condensation. As the electrical power in the evaporator is shut off, the rate of evaporation decreases faster than the rate of condensation. As a result, the vapor travels faster toward the L–V interface along the condenser section, resulting in a rapid decrease in vapor mass in the evaporator and increase in the vapor velocity.

After 2000 s of transient, steady-state operation is established again; however, the temperatures are slightly different from the initial condition. As Fig. 2 shows, the steady-state power throughput is about 13 W, with a centerline vapor velocity of 2.5 m s^{-1} (Fig. 12). Also, Fig. 5 shows a vapor void fraction distribution that is not quite uniform. This is because the temperature is not uniform along the heat pipe. After cooldown, the temperature of the evaporator wall equals room temperature (296.2 K), while the condenser wall is slightly cooler because the cooling water enters the condenser jacket at 294.5 K.

CONCLUSION

A two-dimensional, heat pipe transient analysis model, 'HPTAM', which incorporates liquid com-

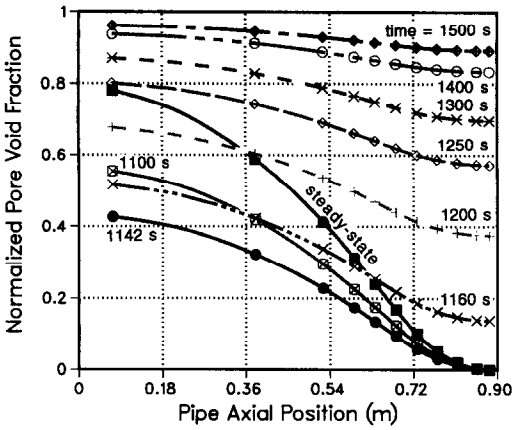

FIG. 10. Calculated axial distributions of the vapor pore void fraction at different times during the cooldown transient of the water heat pipe.

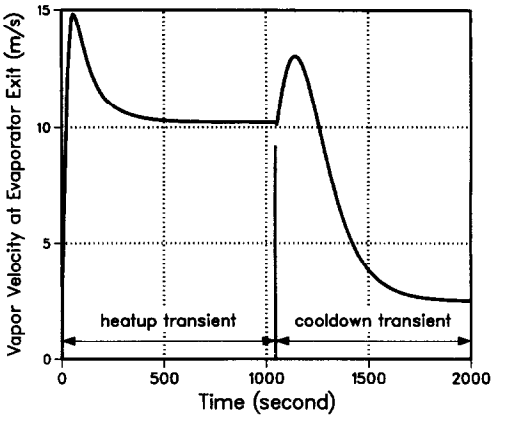

FIG. 12. Calculated centerline vapor velocity at the end of the evaporator as a function of time.

pressibility, energy and momentum discontinuities at the L–V interface, and the capabilities to determine the radius of curvature of the liquid meniscus at the L–V interface and liquid pooling is developed and benchmarked against experimental data of a water heat pipe. The model predictions of the transient values of the vapor and wall temperatures as well as the effective power throughput are in reasonable agreement with experiments. The results show that at steady-state a liquid pool that is 1.7 mm thick forms at the end of the condenser section, where the total vapor and liquid pressures are equal. In addition to water pooling, the transient axial distributions of the vapor and liquid pressures, void fraction in the wick and the effective radius of curvature of the liquid meniscus at the L–V interface are calculated and presented. Also presented is the recession of the liquid pool during the cooldown period of the heat pipe.

Acknowledgements—This research is funded by NASA Lewis Research Center, Grant No. NAG3-941, to the University of New Mexico's Institute for Space Nuclear Power Studies.

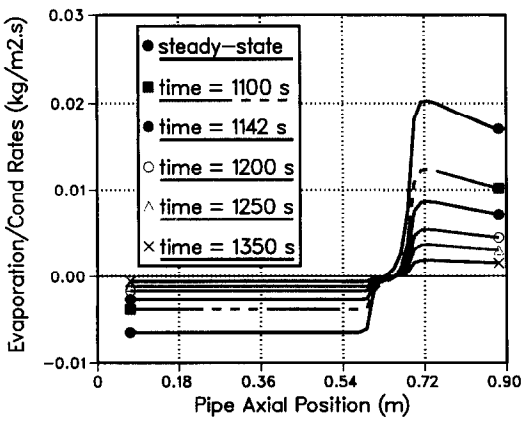

FIG. 11. Calculated axial distribution of evaporation–condensation rates at different times during the cooldown transient of the water heat pipe.

REFERENCES

1. W. J. Bowman and J. E. Hitchcock, Transient compressible heat pipe vapor dynamics, *1988 National Heat Transfer Conference*, Houston, TX, HTD-96, Vol. 1, pp. 329–337 (1988).
2. F. Issacci, I. Catton and N. M. Ghoniem, Vapor dynamics of heat pipe startup, *ASME J. Heat Transfer* **113,** 985–994 (1991).
3. M. N. Ivanovsky, V. P. Sorokin and I. V. Yagodkin, *The Physical Principles of Heat Pipes*. Oxford University Press, New York (1982).
4. D. Tilton, J. Johnson, J. Gottschlich and S. Iden, Transient response of a liquid-metal heat pipe, Air Force Wright Aeronautical Laboratory Report AFWAL-TR-86-2037, Wright Patterson AFB, OH (1986).
5. W. S. Chang and G. T. Colwell, Mathematical modeling of the transient operating characteristics of a low-temperature heat pipe, *Numer. Heat Transfer* **8,** 169–186 (1985).
6. A. Faghri and M. M. Chen, A numerical analysis of the effects of conjugate heat transfer, vapor compressibility, and viscous dissipation in heat pipes, *Numer. Heat Transfer Part A* **16,** 389–405 (1989).
7. Y. Cao and A. Faghri, Transient two-dimensional compressible analysis for high-temperature heat pipes with pulsed heat input, *Numer. Heat Transfer, Part A* **18,** 483–502 (1990).
8. Y. Cao and A. Faghri, Analysis of high-temperature heat pipe startup from the frozen state, *1992 National Heat Transfer Conference*, San Diego, CA, HTD-Vol. 206-3, Topics in Heat Transfer, pp. 89–97 (August 1992).
9. A. Faghri and M. Buchko, Experimental and numerical analysis of low-temperature heat pipes with multiple heat sources, *ASME J. Heat Transfer* **113,** 728–734 (1991).
10. V. H. Ransom and H. Chow, ATHENA heat pipe transient model. In *Trans. of 4th Symposium on Space Nuclear Power Systems*, CONF-870102-Summs., (Edited by M. S. El-Genk and M. D. Hoover), pp. 389–392. ISNPS, UNM, Albuquerque, NM (1987).
11. J. M. Doster and M. L. Hall, Numerical modeling of high-temperature liquid-metal heat pipes, *1989 Joint ASME/A.I.Ch.E. National Heat Transfer Conference*, Philadelphia, Pennsylvania, Vol. 89-HT-13, pp. 1–9 (1989).
12. J. T. Seo and M. S. El-Genk, A transient model for liquid-metal heat pipes. In *Space Nuclear Power Systems 1988* (Edited by M. S. El-Genk and M. D. Hoover), Vol. IX, pp. 405–418. Orbit, Malabar, FL. (1989).

13. M. A. Merrigan, E. S. Keddy and J. T. Sena, Transient performance investigation of a space power system heat pipe, *AIAA/ASME 4th Joint Thermophysics and Heat Transfer Conference*, Boston, MA, paper AIAA-86-1273 (June 1986).
14. J. E. Deverall, J. E. Kemme and L. W. Florschuetz, Sonic limitations and startup problems of heat pipes, Los Alamos Scientific Laboratory Report LA-4518 (accession number N71-18944), Los Alamos, NM (1970).
15. L. Huang, M. S. El-Genk and J.-M. Tournier, Transient performance of an inclined water heat pipe with a screen wick, *1993 ASME National Heat Transfer Conference*, Atlanta, GA, Heat Pipes and Capillary Pumped Loops (Edited by A. Faghri, A. J. Juhasz and T. Mahefkey), HTD-Vol. 236, pp. 87–92 (August 1993).
16. A. E. Scheidegger, *The Physics of Flow through Porous Media* (3rd Edn). University of Toronto Press (1974).
17. P. Cheng, Heat transfer in geothermal systems. In *Advances in Heat Transfer* (Edited by T. F. Irvine, Jr. and J. P. Hartnett), Vol. 14, pp. 1–105. Academic Press, New York (1978).
18. J. M. Delhaye, Local instantaneous equations. In *Two-Phase Flows and Heat-Transfer* (Edited by S. Kakac and T. N. Veziroglu), Vol. 1, pp. 59–79. (*Proceedings of NATO Advanced Study Institute on Two-Phase Flows and Heat-Transfer*, Istanbul, Turkey, August) (1976).
19. C. A. Busse and J. E. Kemme, The dry-out limits of gravity-assist heat pipes with capillary flow, *Proceedings of the 3rd International Heat Pipe Conference*, Palo Alto, paper AIAA-78-383, pp. 41–48 (1978).
20. S. V. Patankar, *Numerical Heat Transfer and Fluid Flow*. Hemisphere Washington, D.C. (1980).
21. R. I. Issa, Solution of the implicitly discretised fluid flow equations by operator splitting, *J. Comput. Phys.* **62,** 40–65 (1986).
22. J.-M. Tournier and M. S. El-Genk, HPTAM, Heat Pipe Transient Analysis Model: an analysis of water heat pipes. In *Proceedings of the 9th Symposium on Space Nuclear Power Systems*, AIP Conference Proceeding No. 246, Part 3, pp. 1023–1037. American Institute of Physics, New York, NY (1992).
23. F. H. Harlow and A. A. Amsden, A numerical fluid dynamics method for all flow speeds, *J. Comput. Phys.* **8,** 197–213 (1971).
24. J. P. van Doormaal and G. D. Raithby, Enhancements of the SIMPLE method for predicting incompressible fluid flows, *Numer. Heat Transfer* **7,** 147–163 (1984).
25. S. W. Chi, *Heat Pipe Theory and Practice*. Hemisphere, Washington, D.C. (1976).